Chapter 2
Dioptrics and Elasticity – Variable Curvature Mirrors (VCMs)

The elastic deformation modes corresponding to the first-order modes of the optical matrix characterizing the wavefront shape are the curvature ($Cv\,1$) and tilt ($Tilt\,1$). These are the two fundamental modes involved in Gaussian optics. Because a tilt is easily obtained by a global rotation of a rigid substrate, this chapter only reduces to mirrors generating a $Cv\,1$ mode. Such *variable curvature mirrors* (VCM) are also sometimes called *zoom mirrors*.

Let us denote $z(r)$ – instead of $w(r)$, because z is usual for representing an optical surface – the optical figure achieved by flexure of a circular plate which is flat at rest. In the thin plate theory, a curvature mode $Cv\,1$ is represented by

$$z \equiv w = A_{20}\, r^2 \equiv \frac{1}{2R}\, r^2 , \tag{2.1}$$

where R is the radius of curvature of the bent optical surface.

Two classes of substrate thicknesses provide the curvature mode as investigated hereafter: Constant thickness distribution (CTD) and Variable thickness distribution (VTD).

2.1 Thin Circular Plates and Small Deformation Theory

2.1.1 Plates of Constant Thickness Distribution – CTD

Let us consider a possibly holed plane circular plate with a constant thickness t and rigidity $D = Et^3/[12(1-\nu^2)] = constant$, where E and ν are the Young modulus and Poisson's ratio, respectively. If an external pair of concentric circle forces or a bending moment are applied to the perimeter region without surface load ($q = 0$), then bilaplacian Poisson's equation representing the flexure z of the plate reduces to

$$\nabla^2\nabla^2 z = 0 , \tag{2.2}$$

whose general solution

$$z = B_{20} + C_{20} \ln r + D_{20}\, r^2 + E_{20}\, r^2 \ln r \tag{2.3}$$

G.R. Lemaitre, *Astronomical Optics and Elasticity Theory,* Astronomy and Astrophysics Library, DOI 10.1007/978-3-540-68905-8_2,

contains the curvature term D_{20}. The external forces taken into consideration by (2.2) can be a central one, a uniform distribution of forces onto a concentric circle, and a uniform radial moment onto the inner and outer edges. Choosing the deformation origin at the plate vertex leads to set $B_{20} = 0$.

We search for external forces and/or radial moments leading to the conditions $C_{20} = E_{20} = 0$. The Laplacian is represented by

$$\nabla^2 z = \frac{1}{r}\frac{d}{dr}\left(r\frac{dz}{dr}\right) = 4\,(D_{20} + E_{20} + E_{20}\,\ln r) \tag{2.4}$$

so the radial shearing force per unit length [cf. (1.187)] is

$$Q_r = -D\frac{d}{dr}(\nabla^2 z) = -4\,E_{20}\,D\,\frac{1}{r}\,. \tag{2.5}$$

Condition $E_{20} = 0$ implies a null shearing force all over the plate, $Q_r = 0$. Therefore, the zeroing of $r^2 \ln r$ coefficient in (2.3) implies that no central force or circle-line force can be applied onto the plate to achieve a $Cv\,1$ mode. From conditions $B_{20} = E_{20} = 0$, the radial bending moment per unit length is

$$M_r = D\left(\frac{d^2 z}{dr^2} + \frac{\nu}{r}\frac{dz}{dr}\right) = D\left[\,2(1+\nu)D_{20} - (1-\nu)C_{20}\,\frac{1}{r^2}\,\right]. \tag{2.6}$$

Coefficients C_{20} and D_{20} are determined from the boundaries, i.e. the bending moments $M_r\{a\}$ at the plate edge and $M_r\{b\}$ at the edge of its central hole. After solving the system, these coefficients are

$$C_{20} = \frac{1}{1-\nu}\,\frac{a^2 b^2\,[M_r\{a\} - M_r\{b\}\,]}{(a^2 - b^2)\,D}\,, \tag{2.7a}$$

$$D_{20} = \frac{1}{2(1+\nu)}\,\frac{a^2 M_r\{a\} - b^2 M_r\{b\}}{(a^2 - b^2)\,D}\,. \tag{2.7b}$$

A pure curvature mode $Cv\,1$ is obtained if the logarithm term vanishes, i.e. if $C_{20} = 0$. From (2.7a), this leads to two solutions: one is with $b = 0$ and the other with $M_r\{b\} = M_r\{a\}$. The coefficient D_{20} is identical for the two solutions which are expressed by

$$B_{20} = C_{20} = E_{20} = 0 \quad \text{and} \quad D_{20} = \frac{M_r\{a\}}{2(1+\nu)D}\,. \tag{2.8a}$$

Finally, by identifying the A_{20} coefficient in (2.1) with D_{20} coefficient, the curvature of the flexure mode $Cv\,1$ is

$$\frac{1}{R} \equiv 2A_{20} = \frac{M_r\{a\}}{(1+\nu)D} = 12\,(1-\nu)\,\frac{M_r\{a\}}{E\,t^3}\,. \tag{2.8b}$$

• **Conclusion for CTD solutions with bending moments**: → *A plate or a slightly curved meniscus generates a* $Cv\,1$ *deformation mode* $z = A_{20}r^2$ *if its thickness* $t = \mathcal{T}_{20}\,t_0$ *is a constant such as*

$$\mathcal{T}_{20} = 1 \quad with \quad \frac{t_0}{a} = \left[6(1-\nu)\frac{M_r\{a\}}{A_{20}Ea^3} \right]^{1/3}, \tag{2.9}$$

and if a bending moment M_r *is applied only. The two solutions providing such a mode for variable curvature mirrors are*:

1. *A plain plate,* $b = 0$*, with uniform bending moment* $M_r\{a\}$ *applied to its edge,*
2. *A holed plate with uniform bending moments* $M_r\{b\} = M_r\{a\}$ *applied to edges.*

From the stress-strain relation one shows that the radial and tangential stresses σ_{rr} and σ_{tt} are equal. Their value are maximum at the surfaces of the plate, i.e. for $z = \pm\, t/2$, and expressed by

$$\sigma_{rr} = \sigma_{tt} = \pm\,\frac{E\,t}{2(1-\nu)R} = \pm\,\frac{6M_r\{a\}}{t^2}. \tag{2.10}$$

The basic solution for a plain plate providing a curvature mode $Cv\,1$ is displayed by Fig. 2.1. Two designs using an outer ring built-in at the perimeter plate are equivalent and allow generating the bending moment by mean of axial forces (Fig. 2.1). The intensity of these forces can be derived from the *vase form* study in Chap. 7.

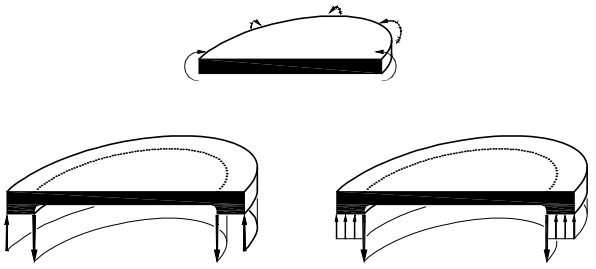

Fig. 2.1 Variable Curvature Mirrors derived from the CTD class. *Up*: Basic solution – uniform bending moment applied along the perimeter, *Down*: Axial forces on a *vase form* providing equivalent bending moments

2.1.2 Plates of Variable Thickness Distribution – VTD – Cycloid-Like form – Tulip-Like Form

Considering variable thickness distributions (VTDs), it is possible to find several configurations which actively generate the first-order curvature mode $Cv\,1$ (Lemaitre [35, 36]). We will see below, from the thin plate theory, that the possible

VTD geometries depend on the load distributions and associated reactions at the substrate boundaries. The radial and tangential bending moments M_r and M_t are represented by

$$M_r \;=\; D\left(\frac{d^2z}{dr^2} + \frac{\nu}{r}\,\frac{dz}{dr}\right), \qquad M_t \;=\; D\left(\nu\,\frac{d^2z}{dr^2} + \frac{1}{r}\,\frac{dz}{dr}\right), \tag{2.11}$$

where $D(r) \;=\; Et^3(r)/[12(1-\nu^2)]$ is the variable rigidity. The static equilibrium between the components M_r, M_t of the bending moments and the shearing force Q_r acting in a plate element is derived about a local tangential axis. This equilibrium writes

$$M_r \;+\; r\,\frac{dM_r}{dr} \;-\; M_t \;+\; r\,Q_r \;=\; 0\,. \tag{2.12}$$

After substitution of M_r, dM_r/dr, M_t and division by $r\,D$, this differential equation becomes

$$\frac{d^3z}{dr^3} + \left(\frac{1}{D}\,\frac{dD}{dr} + \frac{1}{r}\right)\frac{d^2z}{dr^2} + \left(\frac{\nu}{rD}\,\frac{dD}{dr} - \frac{1}{r^2}\right)\frac{dz}{dr} \;=\; -\,\frac{Q_r}{D}\,,$$

that is,

$$D\frac{d}{dr}\,(\nabla^2 z) \;+\; \left(\frac{d^2z}{dr^2} + \frac{\nu}{r}\,\frac{dz}{dr}\right)\frac{dD}{dr} \;=\; -\,Q_r\,. \tag{2.13}$$

Notation (2.1) of a flexural curvature mode leads to $\nabla^2 z = 4A_{20}$. After substitutions, the first derivative of the rigidity is

$$\frac{dD}{dr} \;=\; -\,\frac{Q_r}{2(1+\nu)A_{20}} \;\equiv\; -\frac{R}{1+\nu}\;Q_r\,, \tag{2.14}$$

thus a direct function of the shearing force.

Three loading configurations and boundary reactions on the substrate are of interest for practical applications. Each of them is associated with a particular shearing force.

• **VTD Type 1 – Uniform loading and reaction at edge**: A uniform load q is applied all over the surface of the substrate in reaction at the edge $r = a$. At a current radius r of the substrate, the shearing force is defined by the equilibrium $\pi r^2 q + 2\pi r\,Q_r \;=\; 0$ of the inner element to r, that is

$$Q_r \;=\; -\,\frac{1}{2}\,q\,r\,, \tag{2.15}$$

and after substitution in (2.14), we obtain the rigidity

$$D \;=\; -\,\frac{q\,R}{4(1+\nu)}\,(\mathit{constant} \;-\; r^2)\,.$$

The interest of VTDs is to avoid the application of moments at the boundaries. We can select a null bending moment at the edge, $M_r(a) \;=\; 0$. From (2.11), this is satisfied by taking the rigidity $D(a) \;=\; 0$. Therefore, the rigidity is

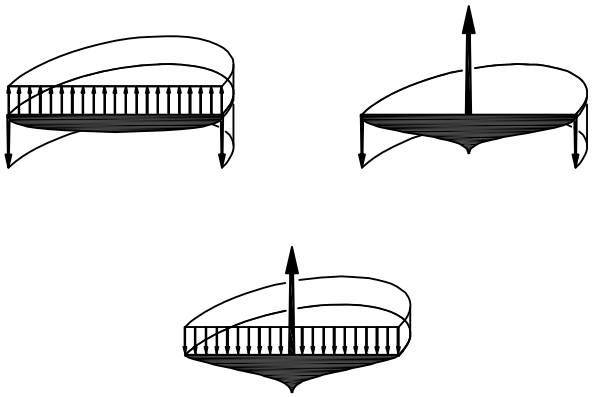

Fig. 2.2 Variable Curvature Mirrors derived from the VTD class. Dimensionless thicknesses $\mathcal{T}_{20}$ with $\rho = r/a$ and $\rho \in [\,0, 1\,]$ (after Lemaitre [35]). *Up-left*: Uniform loading and reaction at the edge, $\mathcal{T}_{20} = (1-\rho^2)^{1/3}$. *Up-right*: Axial force at center and edge reaction, $\mathcal{T}_{20} = (-\ln\rho^2)^{1/3}$. *Down*: Uniform loading and central reaction, $\mathcal{T}_{20} = (\rho^2 - \ln\rho^2 - 1)^{1/3}$

$$D = -\frac{q\,a^2 R}{4(1+\nu)}\left(1-\frac{r^2}{a^2}\right),$$

and the thickness distribution is

$$t = -\left[3(1-\nu)\,\frac{q\,R}{E\,a}\left(1-\frac{r^2}{a^2}\right)\right]^{1/3} a\,.$$

Because of the smoothly decreasing profile for low values of r and vertical tangents at the substrate edge $r = a$, we call this thickness distribution a *cycloid-like form* (Fig. 2.2).

• **Conclusion for VTD solution Type 1**: $\rightarrow$ *Variable curvature mirrors are obtained by uniform loading q and reaction at the edge provided a cycloid-like thickness $t = \mathcal{T}_{20}\,t_0$ is such as*

$$\mathcal{T}_{20} = \left(1-\frac{r^2}{a^2}\right)^{1/3} \quad with \quad \frac{t_0}{a} = -\left[3(1-\nu)\,\frac{q\,R}{E\,a}\right]^{1/3}, \tag{2.16}$$

where $1/R = 2A_{20}$ is the curvature of the deformation, and the product $q\,R$ negative.[1]

At mirror surfaces, the maximum stresses are derived from substitution of the rigidity in the definition of M_r and M_t in (2.11). Their determinations are the following

[1] We will obtain the same VTD for generating the third-order astigmatism mode $Astm\,3$, i.e. $\mathcal{T}_{22} = [1-r^2/a^2]^{1/3}$ where a $\cos 2\theta$ shearing force is now applied to the edge (cf. Sect. 3.5.2). Hence the superposition of both modes $Cv\,1$ and $Astm\,3$ allows, for instance, to generate cylindric-like flexures on mirrors with circular contour (cf. Sect. 3.5.2).

$$\sigma_{rr} \;=\; \pm\,\frac{6M_r}{t^2} \;=\; \pm\,\frac{3}{2}\,\frac{a^2}{t_0^2}\;q\;\mathcal{T}_{20} \;=\; \pm\left[\frac{3}{8(1-\nu)^2}\;\frac{a^2}{R^2}\;qE^2\right]^{1/3}\mathcal{T}_{20}\,, \tag{2.17a}$$

$$\sigma_{tt} \;=\; \pm\,\frac{6M_t}{t^2} \;=\; \sigma_{rr}\,, \tag{2.17b}$$

showing that the radial and tangential stresses are identical $\forall\, r$ – as for a CTD [see (2.10)] – and maximal at the center of the substrate.

• **VTD Type 2 – Axial force at center and reaction at edge**: The substrate is deflected by an axial force F applied to its center that gives rise to a reaction $-F$ at the edge. If we consider an equivalent uniform load q applied to all its surface, we can define the central force by $F \;=\; \pi a^2 q$, and the associated shearing force by $\pi a^2 q + 2\pi r\, Q_r \;=\; 0$, thus

$$Q_r \;=\; -\,\frac{q\,a^2}{2\,r}\,. \tag{2.18}$$

After substitution and integration of (2.14), the rigidity is represented by

$$D \;=\; -\,\frac{q\,R\,a^2}{2(1+\nu)}\,(\,constant\;-\;\ln r\,)\,.$$

Similarly as in the previous configuration, we select a null bending moment at the edge by taking $D_r(a) \;=\; 0$ in (2.11). Therefore, the *constant* = $\ln a$, and the rigidity is

$$D \;=\; -\,\frac{q\,a^2 R}{4(1+\nu)}\left(-\ln\frac{r^2}{a^2}\right).$$

Because of an infinite thickness at $r = 0$ and vertical tangents at the substrate edge, we call this thickness distribution a *tulip-like form* (Fig. 2.2).

• **Conclusion for VTD solution Type 2**: → *Variable curvature mirrors are obtained by axial force F at center and reaction at the edge provided a tulip-like thickness $t \;=\; \mathcal{T}_{20}\,t_0$ such as*

$$\mathcal{T}_{20} \;=\; \left(-\ln\frac{r^2}{a^2}\right)^{1/3} \qquad with \qquad \frac{t_0}{a} \;=\; -\left[3(1\;-\;\nu)\,\frac{F\,R}{\pi\,E\,a^3}\right]^{1/3}, \tag{2.19}$$

where $1/R \;=\; 2A_{20}$ is the curvature of the deformation, and the product FR negative.[2]

---

[2] In the region where the radius r is near the edge radius a, say $0.75 < r/a \leq 1$, we may compare the asymptotic expansion of this VTD with that of Type 1, $\mathcal{T}_{20} \;=\; [1 - r^2/a^2]^{1/3}$, which also allows generating the *Astm* 3 mode. We know that

$$\ln\,x \;=\; x-1\;-\;\tfrac{1}{2}(x-1)^2\;+\;\tfrac{1}{3}(x-1)^3\;-\;\cdots\,, \qquad 0\;<\;x\;\leq\;2\,,$$

which, denoting $\rho \;=\; r/a$, entails for a VTD Type 2

$$(-\ln\,\rho^2)^{1/3} \;=\; \left[\,1-\rho^2\;+\;\tfrac{1}{2}(1-\rho^2)^2\;+\;\tfrac{1}{3}(1-\rho^2)^3\;+\;\cdots\,\right]^{1/3}.$$

• **VTD Type 3 – Uniform loading and reaction at center**: The substrate is deflected by a uniform load q and in reaction at its center by a force $F = -\pi a^2 q$. The associated shearing force at current radius r is defined by the static equilibrium $F + \pi r^2 q + 2\pi r Q_r = 0$, thus

$$Q_r = \frac{q}{2}\left(\frac{a^2}{r} - r\right). \tag{2.20}$$

After substitution and integration of (2.14), the rigidity is represented by

$$D = \frac{q\,R\,a^2}{2(1+\nu)}\left(constant + \frac{r^2}{2\,a^2} - \ln r\right).$$

Similarly as in the previous configurations, we select a null bending moment at the edge by taking $D_r(a) = 0$ in (2.11). Therefore, the *constant* = $1/2\,(\ln a^2 - 1)$, and the rigidity is

$$D = \frac{q\,a^2 R}{4(1+\nu)}\left(\frac{r^2}{a^2} - \ln\frac{r^2}{a^2} - 1\right).$$

Because of an infinite thickness at $r = 0$ and vertical tangents at the substrate edge, this thickness distribution is also a *tulip-like form* (Fig. 2.2).

• **Conclusion for VTD solution Type 3**: → *Variable curvature mirrors are obtained by uniform loading and reaction at the center provided a tulip-like thickness* $t = \mathcal{T}_{20}\,t_0$ *such as*

$$\mathcal{T}_{20} = \left(\frac{r^2}{a^2} - \ln\frac{r^2}{a^2} - 1\right)^{1/3} \quad with \quad \frac{t_0}{a} = \left[3(1-\nu)\,\frac{q\,R}{E\,a}\right]^{1/3}, \tag{2.21}$$

where $1/R = 2A_{20}$ *is the curvature of the deformation, and the product* qR *positive.*

Hence we obtain

$$\lim\left\{\frac{\mathcal{T}_{20\,\text{Type}\,2}}{\mathcal{T}_{20\,\text{Type}\,1}}\right\}_{\rho\to 1} = \lim\left\{\left[1 + \tfrac{1}{2}(1-\rho^2) + \tfrac{1}{3}(1-\rho^2)^2 + \cdots\right]^{1/3}\right\} = 1\,,$$

so the two types are asymptotically the same near the edge. For $\rho = 0.85$, the ratio in the above limit is $\simeq 1.05$.

Since a Type 2 only requires a central force reacting at the edge, when superposing a $Cv\,1$ mode with an $Astm\,3$ mode the number of actuators is lower than for the case of a Type 1 which requires generating an edge-moment, a more difficult condition to achieve in practice. Hence, although theoretically less perfect than for a Type 1, the superposition of $Cv\,1$ and $Astm\,3$ modes with a Type 2 has been proposed by Hugot [24] for telescope integral field units (cf. Sect. 1.12.9). In this development, one may find a more appropriate VTD of the form $\mathcal{T} = \alpha\mathcal{T}_{20\,T1} + (1-\alpha)\mathcal{T}_{20\,T2}$, where $0 \le \alpha \le 1$, which allows us to match the accuracy of both generated modes relative to the wavefront tolerances.

2.1.3 Optical Focal-Ratio Variation

From the three VTDs, we can determine the optical f-ratio variation, i.e. the zoom-range, generated by the $Cv\,1$ deformation of the VCM. Assuming a flat mirror when in an unstressed state, let

$$\Omega \;=\; |f/2a| \;=\; |R/4a| \;=\; |1/8aA_{20}| \tag{2.22}$$

be this f-ratio variation. After substitution, all three VTDs can be expressed by

$$\frac{t}{a} \;=\; \left[12(1-\nu)\Omega\,\frac{q}{E}\right]^{1/3}\mathcal{T}_{20}\,. \tag{2.23}$$

For these distributions, the radial and tangential stresses are identical, $\sigma_{rr} \;=\; \sigma_{tt}$. In practical applications, these stresses must be evidently lower than the tensile maximum stress $\sigma_{T\max}$ of the mirror substrate. Therefore, the maximal value of the stresses σ_{rr} or σ_{tt}, derived from Eqs. (2.17a) and (2.17b), must satisfy

$$\left[\frac{3}{128(1-\nu)^2\Omega^2}\,qE^2\right]^{1/3}\left|\mathcal{T}_{20}\right|_{\max} \;<\; \sigma_{T\max}\,. \tag{2.24}$$

With the tulip-like VCMs, because of the point forces applied at the center, $\mathcal{T}_{20}(0) \to \infty$ in (2.19) and (2.21), and also for the stresses (2.24). In fact, the stem of the profile thickness is very narrow because of its logarithmic nature in $(-\ln\rho^2)^{1/3}$ that comes from the infinite pressure due to the central point-force. For practical applications it is always possible to limit the central thickness to a finite value. The stem truncation is done with respect to the Rayleigh quarter-wave criterion applied to the central area; the axial force is not applied on a point but on a small area, say of typical radius $a/50$.

With the cycloid-like VCM, $|\mathcal{T}_{20}|_{\max} \;=\; \mathcal{T}_{20}(0) \;=\; 1$ from (2.16).

2.1.4 Buckling Instability

A *self-buckling instability* may happen during a curvature change. This is similar to the meniscus shell "jumping toy," in polymer material, which is manually brought, temporarily, to opposite curvature. Avoiding buckling instability requires taking into account the radial tension N_r existing at the middle surface and showing that the maximum compression value of N_r remains small compared to a critical value. This self-buckling instability is avoided by restricting curvatures to always having the same sign during zooming. Furthermore, all three VTDs $\mathcal{T}_{20}$ are decreasing to zero at the edge which also prevents from this instability.

2.2 Thin Plates and Large Deformation Theory – VTD

In the previous Section, the radial and tangential stresses in the middle surface of the plate have not been considered, so that the results are valid only if the sags $a^2/2R$ are small compared to the mean thickness $< t >$ of the substrates. In order to design VCMs generating a large zoom range with the best accuracy, the analysis is deepened by taking into account the strain of the middle surface. As for constant thickness plates (cf. Timoshenko and Woinowsky-Krieger [58]) in the axisymmetric case, the displacement of a point of the middle surface can be resolved into two components: Assuming a plane middle surface before loading, let us denote z, u the axial and radial displacements (instead of using the notation w, u which should be more appropriate for a curved surface at rest). Then, considering the *large deformation theory*, the relative elongations, or strains, in the radial and tangential directions are defined by

$$\varepsilon_{rr} \;=\; \frac{du}{dr} + \frac{1}{2}\left(\frac{dz}{dr}\right)^2, \qquad \varepsilon_{tt} \;=\; \frac{u}{r}\,, \tag{2.25}$$

where the second term of ε_{rr} takes into account the large deformation case, as can be compared with the low deformation strains in (1.109b). The corresponding radial and tangential tensile forces in the middle surface, N_r and N_t per unit length, are defined by

$$\varepsilon_{rr} \;=\; \frac{1}{Et}\,(N_r - \nu N_t)\,, \qquad \varepsilon_{tt} \;=\; \frac{1}{Et}\,(N_t - \nu N_r)\,,$$

which leads to

$$N_r \;=\; \frac{E\,t}{1-\nu^2}\,(\varepsilon_{rr} + \nu\varepsilon_{tt}) \;=\; \frac{E\,t}{1-\nu^2}\left[\,\frac{du}{dr} \;+\; \nu\,\frac{u}{r} + \frac{1}{2}\left(\frac{dz}{dr}\right)^2\right], \tag{2.26a}$$

$$N_t \;=\; \frac{E\,t}{1-\nu^2}\,(\nu\varepsilon_{rr} + \varepsilon_{tt}) \;=\; \frac{E\,t}{1-\nu^2}\left[\,\nu\,\frac{du}{dr} + \frac{u}{r} + \frac{\nu}{2}\left(\frac{dz}{dr}\right)^2\right]. \tag{2.26b}$$

Taking into account the tensile forces (Fig. 2.3) and considering the equilibrium of a segment of dimension dr, $r\,d\theta$ and thickness t, the sum of the projection of theses forces onto the radial direction, after division by $r\,dr\,d\theta$, is

$$N_r \;-\; N_t \;+\; r\,\frac{dN_r}{dr} \;=\; 0\,. \tag{2.27}$$

After calculation of the N_r derivative with respect to z, u, and t, substitution in (2.27) and division by $Etr/(1-\nu^2)$, we obtain the first equation of equilibrium

$$\frac{d^2u}{dr^2} + \left(\frac{1}{t}\,\frac{dt}{dr} + \frac{1}{r}\right)\frac{du}{dr} + \left(\frac{\nu}{t}\,\frac{dt}{dr} - \frac{1}{r}\right)\frac{u}{r} + \frac{1}{2}\left(\frac{1}{t}\,\frac{dt}{dr} + \frac{1-\nu}{r}\right)\left(\frac{dz}{dr}\right)^2 + \frac{d^2z}{dr^2}\,\frac{dz}{dr} \;=\; 0. \tag{2.28}$$

The second equation is given by the equilibrium of the bending moments. This is (2.13) in which Q_r stands for the total shearing force Q_r^* that takes also into

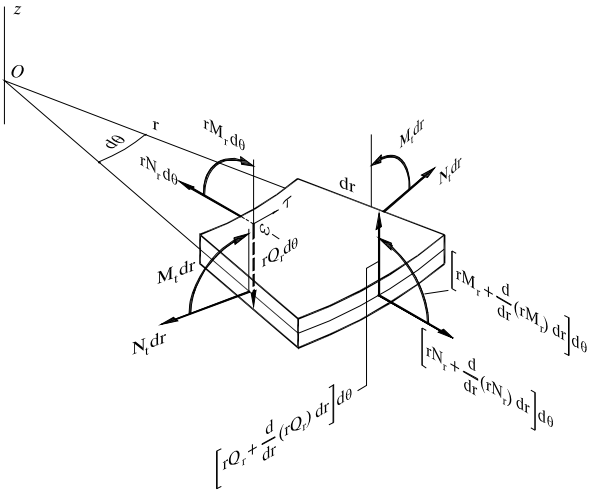

Fig. 2.3 Forces and moments providing the equilibrium of a plate segment

account the axial component of the radial force N_r in the middle surface. The total shearing force Q_r^* is expressed by

$$Q_r^* \;=\; -\,N_r\,\frac{dz}{dr} \;+\; Q_r\;, \tag{2.29}$$

where the shearing force Q_r is defined by the external loading cases in (2.15), (2.18), or (2.20). From the expression of N_r in (2.26a), we obtain

$$\frac{Q_r^*}{D} \;=\; -\,\frac{1}{t^2}\left[\frac{du}{dr} \;+\; \nu\frac{u}{r} \;+\; \frac{1}{2}\left(\frac{dz}{dr}\right)^2\right]\frac{dz}{dr} \;+\; \frac{Q_r}{D}\;. \tag{2.30}$$

After substitution in (2.13), the second equation of equilibrium becomes

$$\frac{d}{dr}(\nabla^2 z) \;+\; \left(\frac{d^2z}{dr^2}+\frac{\nu}{r}\frac{dz}{dr}\right)\frac{1}{D}\,\frac{dD}{dr} \;-\; \frac{1}{t^2}\left[\frac{du}{dr}+\nu\frac{u}{r}+\frac{1}{2}\left(\frac{dz}{dr}\right)^2\right]\frac{dz}{dr} \;+\; \frac{Q_r}{D} \;=\; 0. \tag{2.31}$$

With the hypothesis (2.1) of paraboloid flexure generating a curvature $1/R \;=\; 2A_{20}$ when external forces are applied, and since $dD/D \;=\; 3dt/t$, the substitutions in (2.28) and (2.31) lead to the system (Ferrari [17, 18])

$$\begin{cases} \dfrac{d^2u}{dr^2} \;+\; \left(\dfrac{1}{t}\,\dfrac{dt}{dr}+\dfrac{1}{r}\right)\dfrac{du}{dr} \;+\; \left(\dfrac{\nu}{t}\,\dfrac{dt}{dr}-\dfrac{1}{r}\right)\dfrac{u}{r} \;+\; \left(\dfrac{1}{t}\,\dfrac{dt}{dr}+\dfrac{3-\nu}{r}\right)\dfrac{r^2}{2R^2} \;=\; 0\,, & \text{(2.32a)} \\[2ex] \dfrac{du}{dr} \;+\; \nu\,\dfrac{u}{r} \;-\; 3(1+\nu)\,\dfrac{t}{r}\,\dfrac{dt}{dr} \;+\; \dfrac{r^2}{2R^2} \;+\; 12(1-\nu^2)\,\dfrac{R}{r}\,\dfrac{Q_r}{E\,t} \;=\; 0\,, & \text{(2.32b)} \end{cases}$$

requiring a numerical integration. This was carried out for the design of some VCM with large zoom range.

For each of three VTD types studied in Sect. 2.1.2, the associated shearing force Q_r is expressed by (2.15), (2.18), or (2.20). The boundary conditions are defined by a null thickness at the edge and a finite radial elongation ε_0 at the center

$$\left(t\right)_{r\,=\,a} \;=\; 0\,, \qquad \left(\frac{du}{dr}\right)_{r\,=\,0} \;=\; \varepsilon_0\,. \tag{2.33}$$

Given a VTD type, the integration is carried out by use of dimensionless variables

$$\rho \;=\; \frac{r}{a}\,, \quad U \;=\; \frac{u}{r}\,, \quad \mathcal{T}_{20} \;=\; \frac{t}{t_0}\,, \quad \kappa \;=\; \frac{q}{E}\,, \quad \Omega \;=\; \left|\frac{R}{4a}\right|,$$

where Ω is now the design optimal f-ratio of the zoom range (cf. Sect. 2.6.2). Noticing that $u(0) \;=\; 0$ and considering one of the thicknesses obtained in (2.16), (2.19), or (2.21) from the small deformation theory, we start the integration with $\mathcal{T}_{20}\{\rho_{i\,=\,1}\}$

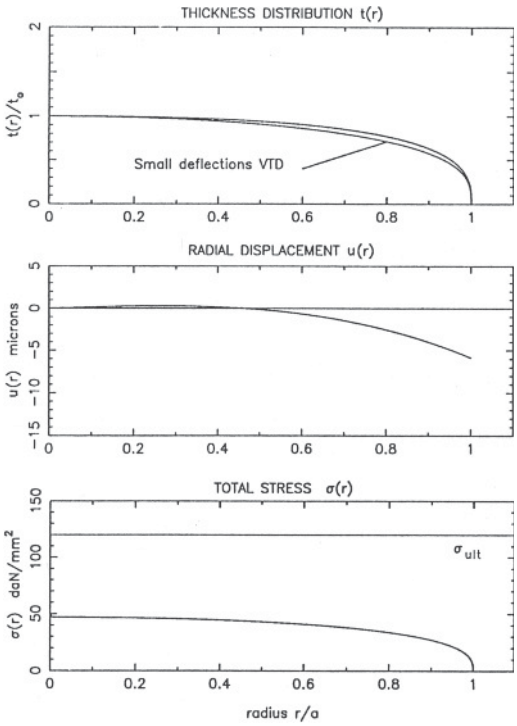

Poisson's ratio	ν =	0.315	Young mod.	E =	2.05 10^6 daN.cm^{-2}
Diameter	$2a$ =	16.00 mm	Uniform load	q =	5.280 daN.cm^{-2}
Central thick.	t_0 =	0.300 mm	Flexural sag	z_0 =	−0.300 mm
Rad. of curv.	R =	−106.6 mm	Max. stress	σ_r =	±50.02 daN.mm^{-2}

Fig. 2.4 Type 1: Uniform loading and edge reaction – Cycloid-like VCM. Results of integration from large deformation theory. Zoom: [f/∞–f/2.5]. The substrate material is Fe87 Cr13 stainless steel alloy in a quenched state (after Ferrari [18])

from one of those equations and inject a value $(dU/d\rho)_{\rho_1} = \varepsilon_0$ unknown, where ρ_1 is small. Equations (2.32b) and (2.32a) provide $d\mathcal{T}_{20}/d\rho$ and $d^2U/d\rho^2$, respectively, the latter gives U_{i+2}. Thus, all elements are known to increment for the next step $\rho_2 = \rho_1 + \delta\rho$ with a very small $\delta\rho$. We can continue the integration in the radial direction by successive increases $\rho_{i+1} = \rho_i + \delta\rho$. Thus, by changing the starting values of the radial elongation ε_0, the numerical process is repeated up to satisfy at edge $\mathcal{T}_{20}\{1\} = 0$.

The maximum radial stresses σ_{rr} on each surface of the substrate is the sum of two components

$$\sigma_{rr} = N_r / t \pm 6 M_r / t^2 . \tag{2.34}$$

Figures 2.4 and 2.5 display the reduced thickness $\mathcal{T}_{20} = t/t_0$, the radial deformation u and the maximum stress σ_{rr} resulting from the integration for a cycloid-like form (VTD Type 1) and a tulip-like form (VTD Type 2). The air pressure load generates convex flexures all over the zoom range. The basic sag used for the integration is

$$z_0 = A_{20}a^2 = a^2/2R = -2a/\Omega , \tag{2.35}$$

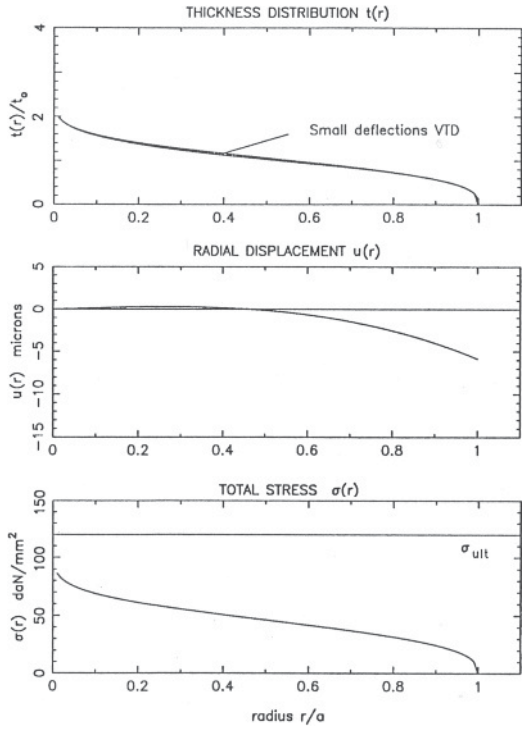

Poisson's ratio	$\nu = 0.315$	Young mod.	$E = 2.05\ 10^6$ daN.cm^{-2}
Diameter	$2a = 16.00$ mm	Uniform load	$F = 9.700$ daN
Central thick.	$t_0 = 0.600$ mm	Flexural sag	$z_0 = -0.400$ mm
Rad. of curv.	$R = -106.6$ mm	Max. stress	$\sigma_r = \pm 116.4$ daN.mm^{-2}

Fig. 2.5 Type 2: Axial force at center and edge reaction – Tulip-like VCM. Results of integrations from large deformation theory. Zoom: [f/∞ – f/2.5]. The substrate material is Fe87 Cr13 stainless steel alloy in a quenched state (after Ferrari [18])

and negative in both cases ($R < 0$, $q > 0$ and $F > 0$). In the integrations for VTDs Type 1 and 2, the thickness distributions are determined for the *basic* f-ratio value f/3.33 considered as the mean value of the zoom range, thus determining z_0. At the limit of the zoom range, the maximum *deformation-ratio* in Type 1 reaches $z_0/t_0 = -1.33$ at f/2.5, i.e. a flexure sag larger than the thickness.

The forces N_r and N_t are both positive at the central zone of the substrate. At the outer part, the force N_r decreases to zero at the perimeter but the force N_t becomes negative. For much larger deformations, this could entail an elastic instability traduced by multiple wavelets along the edge similarly as analytically developed by Casal [7] in his theory of membranes.

The relations between the load q – or central force F – and the deformation-ratio z/t_0 over the zoom ranges [f/∞ – f/2.5] have been determined by Ferrari [20]. These curves show the important non-linearity as well for a VTD Type 1 as for a VTD Type 2 (Fig. 2.6).

From these results, the load q or F can be represented in an odd power series of the deformation ratio z/t_0 by

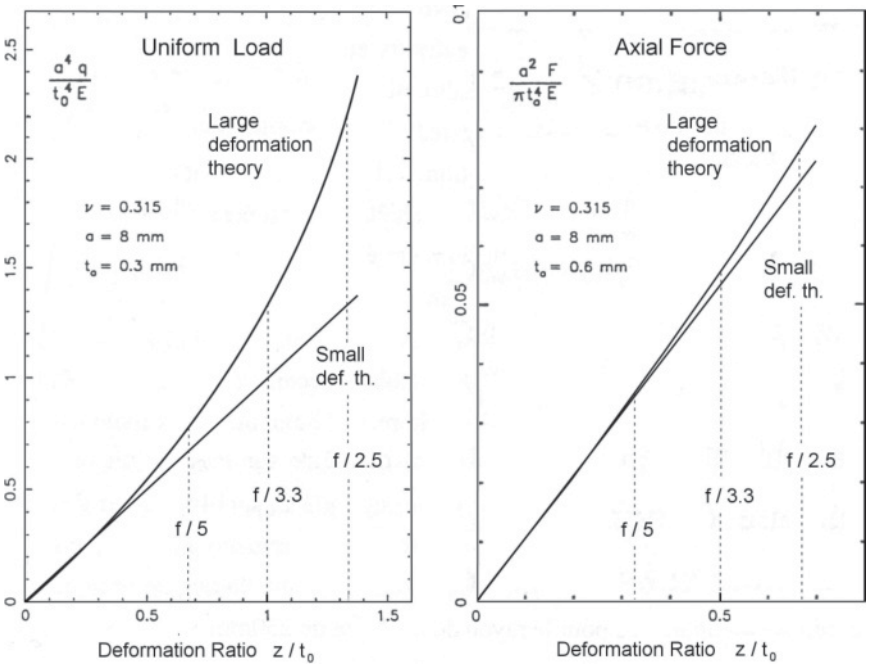

Fig. 2.6 Comparison of dimensionless load-flexure relations. *Left*: VTD Type 1 – Uniform load in reaction at the edge. *Right*: VTD Type 2 – Central force in reaction at the edge

$$\frac{a^4}{t_0^4}\,\frac{q}{E} \equiv \frac{a^4}{\pi t_0^4}\,\frac{F}{a^2 E} = \sum_{i\,=\,1,3,5,\,\ldots} \alpha_i \left(\frac{z}{t_0}\right)^i , \tag{2.36}$$

where α_i are dimensionless coefficients.

2.3 The Mersenne Afocal Two-Mirror Telescopes

The *Mersenne two-mirror telescopes*, published in 1636 [45, 46], are made of two confocal paraboloid mirrors thus providing *afocal systems*.

Let us consider a concave paraboloid primary mirror M_1 of curvature $1/R_1$ and two paraboloid secondary mirrors M_{2a} and M_{2b}, all having their focus located at the origin of a cylindric coordinate frame. Their shape is represented by

$$z_i = -\frac{R_1}{2k_i} + \frac{k_i}{2R_1}\, r^2 , \tag{2.37}$$

where the suffix $i = 1,\ 2a$ and $2b$ characterizes each mirror, and k_i are dimensionless parameters defined by

$$k_1 = 1\,, \quad k_{2a} = \frac{R_1}{R_{2a}} > 0\,, \quad k_{2b} = -\,k_{2a} < 0\,, \tag{2.38}$$

so that the surfaces of M_{2a} and M_{2b} have opposite curvatures $1/R_{2b} = -\,1/R_{2a}$.

Assuming that each side of M_{2a} and M_{2b} mirrors may be used, Mersenne obtained *four* distinct afocal forms (Fig. 2.7).

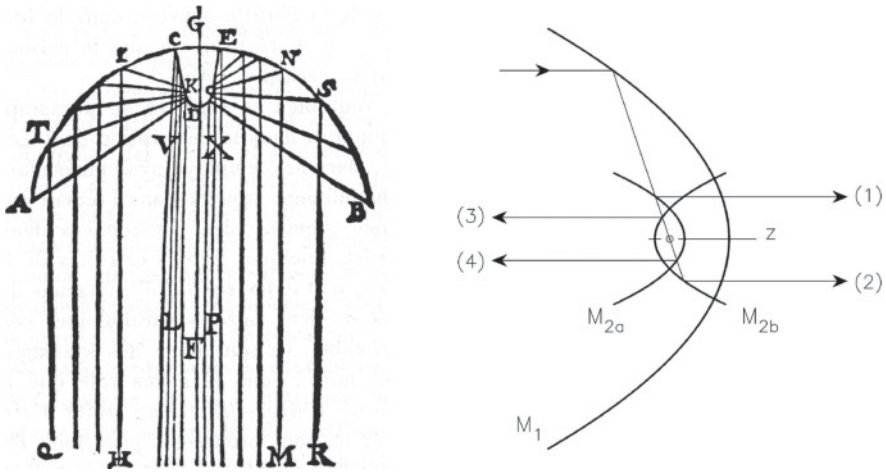

Fig. 2.7 Mersenne afocal two-mirror telescopes. *Left*: One of the four forms proposed by Mersenne in 1636 [45]. *Right*: The four forms

- FORM 1 uses the convex side of M_{2a} mirror (Cassegrain form),
- FORM 2 uses the concave side of M_{2b} mirror (Gregory form),
- FORM 3 uses the convex side of M_{2b} mirror (retro-reflective form),
- FORM 4 uses the concave side of M_{2a} mirror (retro-reflective form).

Forms 1 and 2 (see also Fig. 1.6) may be used in the paraxial zone as well as in grazing incidences for both mirrors. Retro-reflective forms 3 and 4 preferably applies to rays with large heights at the primary corresponding to conjugates with low heights at the secondary and conversely; however the third-order aberration theory that uses the classical Hamilton/Seidel formulation [53] may not be able to correctly model those two latter forms.

Denoting in a general formulation

$$k \;=\; R_1/R_2 \tag{2.39}$$

the algebraic radius ratio of the two mirrors, and h the height of an incident ray, it can readily be shown that the conjugate height h' of the system emerging ray is a solution of

$$h'^2 \;-\; \left(h - \frac{R_1^2}{h}\right)\frac{h'}{k} \;-\; R_2^2 \;=\; 0\,, \tag{2.40}$$

from where the roots may be written as

$$\begin{cases} \dfrac{h}{h'} \;=\; k \;=\; constant \quad \text{for} \quad \begin{cases} \text{Form 1} \\ \text{Form 2} \end{cases} & \text{(2.41a)} \\[2ex] h\,h' \;=\; -\,\dfrac{R_1^2}{k} \;=\; constant \quad \text{for} \quad \begin{cases} \text{Form 3} \\ \text{Form 4} \end{cases} & \text{(2.41b)} \end{cases}$$

With the two first forms, the heights of emerging rays vary in accordance with (2.41a) as an *homothetic transformation congruence* of the Gaussian optics type. With the two latter *retro-reflective systems*, the emerging rays get closer to the telescope axis if the incident ray moves away from the axis. These heights vary in accordance with (2.41b) that we call an *inversion transformation congruence* of the conjugate heights; this latter case was certainly remarked by Marin Mersenne who displayed numerous rays in his figure – actually Fig. 2.7–*Left* – of *Harmonie Universelle* (1636).

The four Mersenne forms are free from all order spherical aberration; thus, in the third-order Seidel theory, the first sums relative to *Sphe* 3 are

$$\mathbf{\Sigma}_1\, S_I \;=\; \mathbf{\Sigma}_2\, S_I \;=\; (\mathbf{\Sigma}_3\, S_I) \;=\; (\mathbf{\Sigma}_4\, S_I) \;=\; 0\,, \tag{2.42}$$

where the parentheses point out that, because of the inversion transformation congruence between the input and output conjugate rays, actually these sums cannot be properly derived from this theory for Mersenne forms 3 and 4; in some optical design codes, the selection of the second alternative intersection point of an optical

surface is achieved by a special option as "alternate even" in Zemax. For instance even for an extremely small field of view – typically of 1 or 10 arcsec – raytraces with Mersenne form 3, $k = -2$, and linear central obstructions of 0.3 or 0.4, show *huge* field aberrations; when anastigmatically focalized, the residual blur images show a remarkable *rotational* symmetry.

• **Quasi-perfect two-mirror systems**: Restraining only to the Mersenne afocal forms 1 and 2, we must mention that for three and a half centuries, *all* of the additional properties of these systems remained unknown. We now know that they are remarkable *anastigmatic systems*, i.e. also free from *Coma* 3 and *Astm* 3,

$$\mathbf{\Sigma}_1 S_{II} = \mathbf{\Sigma}_2 S_{II} = \mathbf{\Sigma}_1 S_{III} = \mathbf{\Sigma}_2 S_{III} = 0\,, \tag{2.43}$$

and that *Dist* 3 can be cancelled, $\mathbf{\Sigma}\, S_V = 0$, if the input pupil is conveniently located.

Astonishingly on may notice, first, that the aplanatic property of these two simple systems has *not* been clearly understood, say, up to the 1960s. Second, the demonstration of the anastigmatic property came much later.[3]

The *Petzval theorem* or Seidel sums $\mathbf{\Sigma}\, S_{IV}$ allow deriving the Petzval curvature (cf. Sect. 1.10.1). For Mersenne form 1 or 2, the *Petz* 3 curvature is also the field curvature. Whatever the position of the pupil and mirrors, for a two-mirror system this curvature is

$$1/R_P = -2/R_1 + 2/R_2\,, \tag{2.44}$$

which entails that the absolute value of the Petzval curvature is the smallest for any Cassegrain form, thus for Mersenne form 1.

A generalized Schwarzschild theorem formalized by Wilson [62] states that

→ *n separated aspheric mirrors or lenses in any geometry allow the correction of n conditions.*

It must be added that some particular geometries are more favorable than others.

For instance, the particular confocal geometry of *Mersenne forms* 1 *and* 2 provides the correction of the three conditions $\mathbf{\Sigma}\, S_I = \mathbf{\Sigma}\, S_{II} = \mathbf{\Sigma}\, S_{III} = 0$ with only two aspherical surfaces and then are absolutely fundamental optical systems. Because also correcting the spherical aberration and linear coma at *all* aberration orders, the Mersenne two-mirror systems are important designs for the development of 3-, 4- and 5-mirror telescopes.

[3] Although the Seidel theory has been well established since the 1860s, the *aplanatism* property of a confocal Mersenne mirror-pair seems to have been only remarked in the 1960s probably from raytrace designs of long-slit spectrographs for telescope prime focus. The complete demonstration of the *anastigmatism* property seems to have been first given by Martin Krautter [29] in 1986 by use of coefficients first formalized by Schwarzschild in his general aberration theory of a two-mirror telescope (1905). Using the Seidel sums, other demonstrations of the anastigmatism were later given by D. Korsch [28] and with a more classical formalism by R. Wilson [62].

It is surprising for those who know the work of M. Paul in 1935 [51] that he did not at that time, in setting up his well-known anastigmatic three-mirror telescope, depart from the principle of the Mersenne telescope. Instead, he derived his telescope form from a paraboloidal primary corrected by an afocal field corrector consisting of two separated mirrors. It is clear he was referring in no way to the properties of Mersenne telescopes.

Another special case is the remarkable geometry of the *flat-field anastigmat three-mirror Rumsey telescope* [52] where M_1-M_2 is a quasi-confocal pair allowing the system to satisfy the four conditions $\mathbf{\Sigma}\, S_I = \mathbf{\Sigma}\, S_{II} = \mathbf{\Sigma}\, S_{III} = \mathbf{\Sigma}\, S_{IV} = 0$ with only three aspherical mirrors. In a modified design, a Rumsey-Lemaitre telescope [39] was built by active optics methods starting from the *same* sphere for M_1 and M_3 mirrors that are both on a single substrate, thus aspherizing the three surfaces of the telescope by only figuring two stressed *spherical* surfaces (see Sect. 6.6.7 for the aspherization of the M_1-M_3 double vase form mirrors and Sect. 3.3.5 for that of the M_2 tulip form mirror).

2.4 Beam Compressors, Expanders and Cat's Eyes – Active Optics Pupil Transfers

Two-arm interferometers developed for high spatial or high spectral resolutions, require the use of *retro-reflective systems*. Because retro-reflective Mersenne telescopes (forms 3 and 4) cannot be used with all rays in the paraxial space [cf. Sect. 2.3 (2.41b)], then considering the Mersenne anastigmat of Gregory type (form 2) having real intermediate focus, we may obtain a *retro-reflective system* by addition of a mirror M_2 at the common focus of M_1 and M_3 paraboloids (Fig. 2.8). When M_2 deviates from a flat shape, the system is no longer anastigmatic but remains *aplanatic*.

Such a three-mirror *beam compression system* or a *beam expander system* can also be characterized by its compression ratio. The form corresponding to a compression ratio equal to unity is called a *cat's eye system*. If mirror M_2 is a VCM, then the system allows an *active pupil transfer*.

Let us define the beam compression ratio by $k = R_1/R_3$. Considering retro-reflective forms for which always $k > 0$, a coordinate system with its origin at the vertex of the M_1 mirror – $f_i = R_i/2$ are all negative in Fig. 2.8 – and an object pupil at abscissa p_1, the conjugate distance equation

$$(p'_1 - f_1)(p_1 - f_1) = f_1^2 \,, \tag{2.45}$$

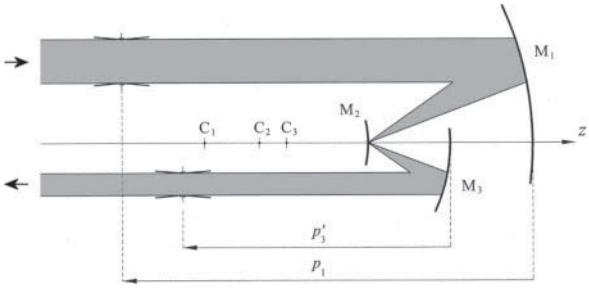

Fig. 2.8 Active pupil transfer by VCM-M_2 retro-reflective systems. These systems are aplanats if M_1 and M_3 are confocal paraboloids

provides the abscissa of the pupil image p'_1. Translating the system origin to the vertex of M_2, this image pupil corresponds to an object pupil of abscissa p_2. The passing equation is $p_2 = p'_1 - f_1$ which provides the image pupil p'_2 by using the conjugate distance equation of M_2

$$p'_2 = \frac{f_2^2}{\dfrac{f_1^2}{p_1 - f_1} - f_2} + f_2 .$$

Finally, from the passing equation $p_3 = p'_2 + f_3$, the abscissa p'_3 of the output pupil with respect to p_1, in the M_3 frame, is

$$p'_3 = \frac{f_3^2}{\dfrac{f_2^2}{\dfrac{f_1^2}{p_1 - f_1} - f_2} + f_2} + f_3 ,$$

thus after transformation,

$$p'_3 = -\left(\frac{f_3}{f_1}\right)^2 p_1 + \left(1 + \frac{f_3}{f_1} + \frac{f_3}{f_2}\right) f_3 , \tag{2.46}$$

where $f_3/f_1 = 1/k$ is the reciprocal beam compression ratio.

For *retro-reflective beam compressors*, the pupil conjugate distances are with $k > 1$.

For *retro-reflective beam expanders*, the pupil conjugate distances are with $0 < k < 1$.

For *retro-reflective cat's eyes*, $k = 1$, the sections of input and output beams have an identical size since paraboloids M_1 and M_3 are coinciding, $R_3 = R_1$. Thus, the conjugate distances of the pupils p_1 and p'_3 with respect to the vertex of the M_1 mirror are linked by

$$p'_3 = -p_1 + \left(2 + \frac{f_1}{f_2}\right) f_1 . \tag{2.47}$$

When the VCM M_2 has a plane shape, $R_2 = \infty$, this formula reduces to $p_1 + p'_3 = 2f_1$. In this case, if $p_1 = f_1$, then $p'_3 = f_1$: $\rightarrow$ Both input and output pupils are at focus abscissa.

The aplanatic properties of these retro-reflective systems are useful in high-resolution interferometry which always requires a small field of view.

2.5 VCMs as Field Compensators of Interferometers

A VCM installed at the focal plane of a cat's eye system allows us to control the output pupil distance and to maintain it at a convenient location where the beams are recombined. At the same time, the pupil conjugation provides the convenient

correction of optical paths in the field of view, so that these systems are also *field compensators*.

Fourier transform spectrometers and telescope array interferometers require VCMs that are used by *active optics control systems*.

2.5.1 Fourier Transform Spectrometers

Two-arm interferometers are particularly useful for the spectral analysis in the infrared and far-infrared - typically in the range 1–20 μm. A plane parallel plate splits the collimated beam into two channels as with a Michelson-type interferometer. The translation of one arm provides a variation of the optical path difference. After recombination, the beams are imaged on a monopixel detector. The spectral recording is achieved by measuring the intensity of the resulting interferences during the arm translation; then, the spectrum is obtained by calculations using a Fourier transform analysis. The largest Fourier transform spectrometers (FTSs) were built by the Laboratoire de Physique Moleculaire et Applications (LPMA) of the University Pierre and Marie Curie, Paris (Fig. 2.9).

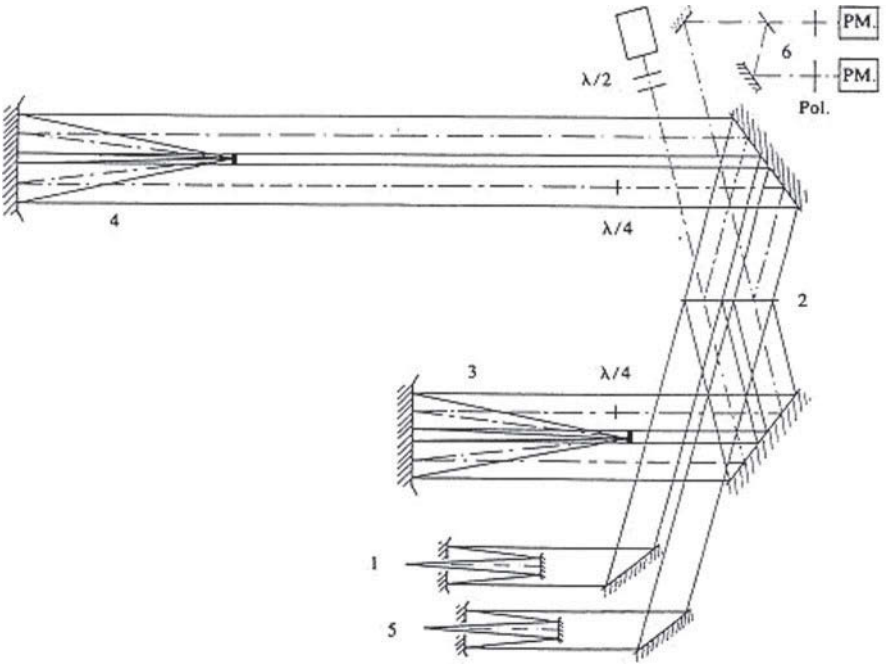

Fig. 2.9 Optical design of the Large FTS at Jussieu LPMA. The maximal optical path difference is 22 m. 1 – Infrared source and collimator, 2 – Beam splitters, 3 – Fixed cat's eye, 4 – Movable cat's eye with VCM, 5 – Camera optics and detector, 6 – Control of path difference by He-Ne laser (– · – · –) (after Valentin [60])

FTSs have been proposed and developed by Jacquinot [25, 26] in order to achieve high spectral resolutions without requiring use of diffraction gratings. Although some FTS concepts not requiring use of on-line computation – by recording stationary interferences on holographic plates – have been proposed and built (Stroke [56]), most instrument concepts are based on a multiplex computational analysis.

In the astrophysical case, high-resolution FTSs have been built for infrared studies of the Sun, Jupiter, and Saturn at Meudon, at McMath-Pierce Solar Telescope of the National Solar Observatory (NSO) and other institutes (Connes [9], Brault [5]), and lower-resolution FTSs for infrared studies of stars (Maillard [41]). In the case of molecular physics studies at the laboratory, very high resolution FTSs have been built (Valentin [60]). Recent developments of FTS methods have led to a large variety of instruments, each of them being specialized to the physics study of a particular problem (see Bracewell [4], Mertz [47], Thorne [57], Smith [54], Davis [11], Christy et al. [8]).

Compact FTSs for broadband studies have proved useful by use of 1D and 2D detectors. A FTS concept with a 1D detector and slightly tilted mirrors (Dohlen [14]) can be used without translation of a mirror; the same design with a 2D detector provides the long slit mode (Dohlen [15]). Replacing the Michelson mirrors by diffraction gratings (Dohi and Suzuki [13]), a 2D detector also allows the fast recording of a temporal chemical reaction, similar to the conventional long slit mode. These instruments do not need to vary the optical path and all optical pieces are statics.

In using 2D infrared detectors and varying the optical path, cat's eye FTSs provide 3D super-imaging and become integral field spectrometers similar to integral field spectrographs in the visible (cf. Sect. 1.12.9), but with the advantage of a free spectral resolution, i.e. which is not preselected by the optical design. 3-D or super-imaging FTSs have been developed at CFHT by Maillard [42] for observations in the spectral range 1–5 μm.

VCM and cat's eye systems were originally developed by Lemaitre in 1975 (cf. Connes and Michel [10]) for the mobil arm of the FTS of Aimé Cotton Laboratory in Bellevue. Such a system was recently implemented on the Large FTS of the Molecular Physics Laboratory and Applications (LPMA) at University P. and M. Curie, Paris-Jussieu, by Valentin and Henry [61] (see Fig. 2.9).

For large optical path variations ($\Delta\ell = 22$ m at Jussieu LPMA) in dual arm interferometers, thus providing high spectral resolutions in the infrared, a *VCM and cat's eye system* allows a substantial increase in luminosity and S/N ratios. This is due to the gain on the *optical Étendue* which is typically increased by a factor of 100.

2.5.2 Stellar Interferometers and Telescope Arrays

Following Young's and Fizeau's ideas of observing interferences from the light of a single wavefront passing through a pair of holes, interferometric methods have been developed in astronomy for the measurement of stellar diameters. The first approach

used two sub-apertures (lunules) oppositely separated at a 65 cm distance on the 80-cm Foucault telescope; although the small size of the subapertures overcame the degradation of the atmospheric seeing, Stephan [55] deduced in 1873 that his optical baseline was too small to observe a fringe pattern which related to an angular star diameter and rightly concluded that the diameters of proximate bright stars are smaller than 0.15 arcsec. The first measurements of stellar diameters – 0.05–0.04 arcsec – where obtained by Michelson [48] by using two aperture mirrors of larger baseline mounted and driven by the 100-inch Mount Wilson Telescope. This class of interferometers has been developed to resolve stellar diameters up to 0.02 arcsec.

Another class of stellar interferometers has been developed by recombining the beams of a pair of telescopes, thus allowing a longer baseline and corresponding higher resolutions. Progress in pointing accuracy and cell sensitivity led Hanbury Brown [6] to resolve star diameters up to $0.7\,10^{-3}$ arcsec with two radio-telescopes and intensity correlation methods. Progress in 2D detectors for the visible and laser positioning control allowed Labeyrie [32, 33] to coherently recombine two optical telescopes (I2T), thus, opening the way to telescope arrays.

By using a sufficiently large number of unit telescopes, a telescope array allows to us recover the high-resolution imaging that should be provided by a monolithic telescope of the same aperture as the baseline. By increasing the amount of light with large unit telescopes, telescope arrays joined to adaptive optics compensations allow the study of much fainter objects. Giant baselines are planned for use in space where diffraction limited images are immediately available. For ground based astronomy, the remarkable advance realized with GI2T by Vakili and Percheron [59] and Mourard et al. [49] has led astronomers to develop the array concept in symbiosis with those of very large telescopes.

The construction by the European Southern Observatory (ESO) of the Very Large Telescope (VLT) and its associated Interferometer (VLTI) realizes a symbiosis approach in combining deep field programs, high-resolution imaging, and interferometric programs by implementation of four 8 m unit telescopes and several auxiliary telescopes. The main features of the ESO interferometric array have been developed and described in Woltjer et al. [63], Beckers [1–3], Merkle [44], von der Lühe et al. [30, 31], Mariotti et al. [43], Glindeman et al. [23], Koehler and Flebus [27] (Fig. 2.10).

The VLTI was designed for recombining the light of four 8 m unit telescopes and four 1.8 m auxiliary telescopes. This is the first telescope array allowing a *field compensation*, sometimes called *field cophasing*. Eight delay lines equipped with cat's eye carriages by Derie [12], allow us to maintain the equality of optical paths during the interferometric acquisitions at the recombining laboratory (Fig. 2.11).

Starting to operate in 2006, the VCMs provide a compensation over 2-3 arcsec sky field diameter (Ferrari et al. [19]). Each VCM is installed at the Cassegrain focus of a translating f/1.6–f/6.5 Ritchey-Chrétien telescope of 550 mm clear aperture. Such cat's eye systems open the way to dual object studies with large format detectors (Leinert and Graser [34], Paresce et al. [50]). Each VCM provides the control of the pupil transfer to the recombination laboratory. With a large zoom range [f/∞–f/2.5], the convex curvatures of the VCMs are in closed-loop control with

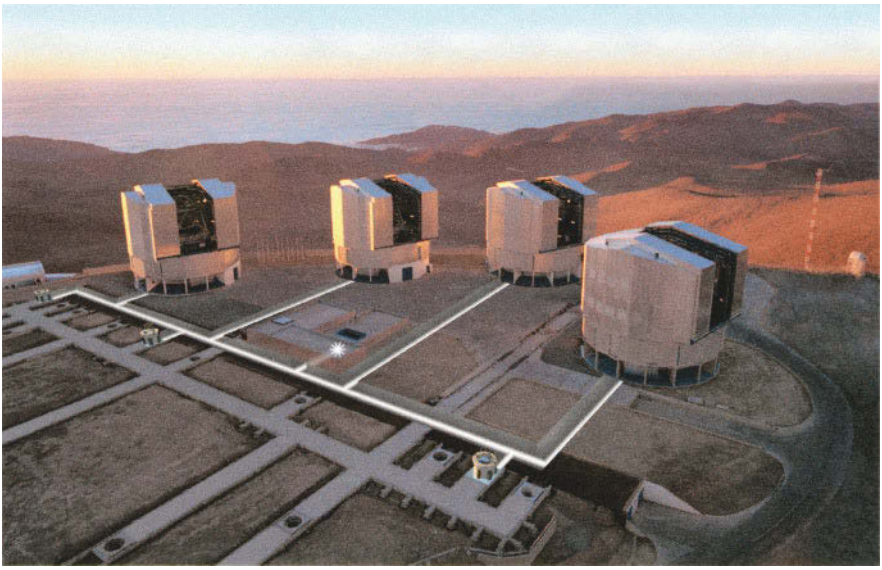

Fig. 2.10 View of the VLT Interferometer at Cerro Paranal (courtesy ESO)

Fig. 2.11 Views of VLTI delay lines and translation cat's eye (courtesy ESO). The cat's eyes are Ritchey-Chrétien telescopes with a VCM at focus (after F. Derie [12])

the location of the cat's eye carriages. A carriage translation can compensate for optical-path differences up to 120 m.

2.6 Construction of VCMs with VTDs

2.6.1 Elastic Deformability and Choice of Material Substrate

In active optics applications, an important choice is that of the material. This material must be extremely linear, in the sense of Hooke's law of a linear stress-strain

relationship. Glass, vitro ceramics and some metal alloys possess this linear characteristic. If large deformations are required, an additional important feature is the *elastic deformability ratio*.

To define this quantity, one may express the parabolic flexure which corresponds to the curvature mode $Cv\,1$ as a function of physical quantities depending on the substrate material. For this, one may use either constant thickness distribution (CTD) or variable thickness distribution (VTD) mirrors. For instance, from (2.1), and (2.8b) (2.10) for CTD, the flexure can be represented as

$$z \;=\; \frac{1}{2R}\, r^2 \;=\; \pm\,(1-\nu)\,\frac{|\sigma|}{E\,t}\, r^2, \tag{2.48a}$$

where the positive sign is for $R > 0$ and from which the sag at mirror full aperture is

$$z\{a\} \;=\; \pm\,(1-\nu)\,\frac{|\sigma|}{E}\,\frac{a^2}{t}\,, \tag{2.48b}$$

where $\sigma \;=\; \sigma_{rr} \;=\; \sigma_{tt}$ are the stresses arising at the surfaces of the plate. We would obtain, for instance, an identical result for a Type 1 VTD mirror which shows a continuous thickness t_0 at center so that now $t \to t_0$ in (2.48b), the stress σ arising in the plate is for $r \;=\; 0$ and is the same as before in CTD.

From material mechanical testing, it is well known that the *tensile* ultimate stress is much lower than the *compression* ultimate stress. Let $\sigma_{T\max}$ be the *tensile maximum stress* of a material as an acceptable limit that must not be exceeded to avoid rupture or plastic strain. Since a tension σ is positive in our sign convention, from (2.48b), and given a plate of diameter $2a$ and thickness t, the *elastic deformability ratio* of a material may be characterized by the dimensionless quantity

$$(1-\nu)\,\frac{\sigma_{T\max}}{E}\,. \tag{2.48c}$$

As most materials used in active optics have a Poisson's ratio $\nu \in [\,0.11,\ 0.33\,]$, it is more convenient to simply define the elastic deformability as

$$\text{elastic deformability} \;=\; \frac{\sigma_{T\max}}{E}\,. \tag{2.48d}$$

For instance from Table (1.10), comparing a Zerodur vitroceram (where $\sigma_{t\,\max} \;=\; 22\,\text{MPa}$ and $E \;=\; 90.2\,\text{GPa}$), with a quenched stainless steel Fe87 Cr13 (where $\sigma_{t\,\max} \;=\; 1.4\times 10^3\,\text{MPa}$ and $E \;=\; 201\,\text{GPa}$), the gain in elastic deformability is $\sim$28-times in favor of this metal alloy; taking into account the Poisson ratio would lead to a gain $\sim$25.

Other linear alloys usable for mirrors, such as Ti90Al6V4 or Be95Cu5, could also provide large gains in elastic deformability, but their practical machining to the convenient geometry of a VTD seems more difficult. For large zoom range VCMs, stainless steel Fe87 Cr13 in a quenched state has been found preferable.

2.6.2 Zoom Range and Choice of a Thickness Distribution

For a small zoom range, the design of a VCM using a VTD is straightforward. With the examples in Fig. 2.6, if the zoom range is corresponding to a variation of [f/∞–f/7] with VTD Type 1 or a variation of [f/∞–f/5] for VTD Type 2, the stress-strain relations are quasi-linear and any thickness profile $\mathcal{T}_{20}$ provides accurate curvatures which are *affine paraboloids*.

For a large zoom range such as [f/∞–f/2.5], it is not possible to obtain affine paraboloids all over the range. Assuming that the VCM is polished flat or slightly convex at an f-ratio Ω_0 close to infinity when at rest, and that the zoom range varies down to $\Omega_{\min}$, a balance of the surface deviation to a paraboloid can be obtained if the thickness $\mathcal{T}_{20}$ is determined for an Ω-value such as $\Omega \in [\,\Omega_0, \Omega_{\min}\,]$. In this range the full sag variation is subdivided into four equal segments and the optimal design f-ratio Ω for the calculation of $\mathcal{T}_{20}$ is determined for the junction of the last two segments by using the balance criterion

$$\frac{1}{\Omega} \;=\; \frac{1}{\Omega_0} + \frac{3}{4\,\Omega_{\min}}\;. \tag{2.49}$$

Therefore with a flat or quasi-flat VCM at rest, i.e. $\Omega_0 \simeq \infty$, this criterion for the determination of $\mathcal{T}_{20}$ means that the mirror is a paraboloid when at f/Ω, while maximum spherical aberration residuals of the optical surface occur with opposite signs at ∼f/$2\Omega_{\min}$ and f/$\Omega_{\min}$.

2.6.3 Achievement of Boundary Conditions

Considering the VTD class, the boundary condition at the VCM perimeter is a free supported edge for Type 1 and Type 2, and free edge for Type 3. From (2.34), no radial bending moment and no radial tension must be applied,

$$M_r(a) \;=\; 0 \quad \text{and} \quad N_r(a) \;=\; 0\,.$$

With metal mirrors, taking into account that only the axial reaction acts at the edge of Type 1 and Type 2, these conditions can be approximated by using a small cylindric collaret that links the VCM to an outer thick ring (Fig. 2.12). Convenient axial length and radial thickness of the collaret can be defined with respect to the thickness $\mathcal{T}_{20}$ at the edge proximity, for instance from the value of $\mathcal{T}(0.99)$.

Because of the instable equilibrium of the acting forces in Type 3, the boundaries only require the VCM to be radially maintained into an outer ring. Since there is no reaction exerted to the edge, a possible solution is to use a very thin linking plate at the edge proximity and compensate for the sag by axial displacement of the zone of central contact during the deformation. Although these boundaries are difficult to fulfill, the comparison of the dimensionless thicknesses displayed by Fig. 2.2 shows

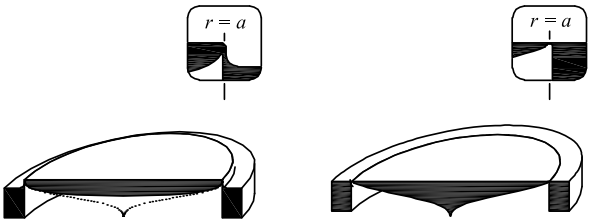

Fig. 2.12 Holosteric solutions linking active substrate and outer ring. *Left*: VTDs Type 1 and 2: Boundaries achieved by a thin cylinder. *Right*: VTD Type 3: Boundaries achieved by a thin plane plate

that Type 3 VCMs are much thinner towards the edge. Therefore compared to Type 1 and 2, Type 3 VCMs are less sensitive to surface deviations from the paraboloid shape and should theoretically provide largest zoom ranges.

2.6.4 Design and Results with VTD Type 1 – Cycloid-Like Form

Type 1 VCMs have been built for optical telescope array interferometers and Fourier transform spectrometers (Ferrari et al. [21]). The following results are obtained with the design parameters of Fig. 2.4 and a thickness distribution $\mathcal{T}_{20}$ determined for f/Ω = f/3.33 allows optimizing the zoom range [f/∞–f/2.5]. An air pressure load generates convex shapes. The substrate is a stainless steel Fe87 Cr13 quenched at a Brinell hardness BH = 330. The integration of system (2.32) provides the dimensionless thickness $\mathcal{T}_{20}$ and then thickness t. A small positive lens-like thickness is added to t in order to compensate for the plastic deformation resulting from the prestressing. The resulting thickness $t^*(r)$ was executed by a numeric command lathe on the rear face of the substrate (Table 2.1).

The prestressing was carried out by slightly overpassing the maximum curvature of the zoom-range (cf. next Section). After prestressing and final plane resurfacing, the mean aspect-ratio of these VCMs may be approximated by $< t > /D \simeq 1/60$. He-Ne interferometric tests were carried out by use of Fizeau lenses of various curvatures and an accurate pressure gauge of resolution 10^{-4} (Fig. 2.13).

Table 2.1 Thickness $t^*(r)$ of a Type 1 VCM before plane surfacing. ESO VLTI and Jussieu LPMA: Zoom range [f/∞–f/2.5]. At VCM edge, the radial thickness of the cylinder-collaret is 25 μm. t^* is with a 18 μm extra-thickness at center which includes a 14 μm positive lens-like shape for plasticity correction (see Sect. 2.7) (LOOM)

r	0	1	2	3	4	5	6	7	7.9	8^+	12
t^*	318	316	311	301	286	265	235	188	150	5,000	5,000

[r: mm, t^*: μm]

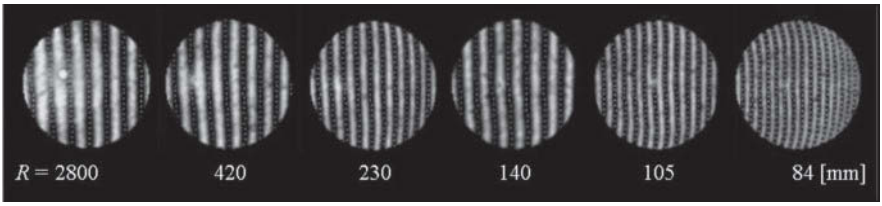

Fig. 2.13 Optical tests of a Type 1 VCM with respect to concave calibers. Fizeau interferograms for a clear aperture $2a = 5$ mm (LOOM)

2.6.5 Design and Results with a VTD Type 2 – Tulip-Like Form

Type 2 VCMs have been built for particular applications where discrete curvatures are preferred to a continuous variation of the curvature (Lemaitre [37]). The central force is generated by a motorized lead screw. These actuators are less complex to use than air pressure units with controller but may provide some vibrations during the zooming. Tulip-like VCMs are useful for pre-positioning the first pupil of telescope arrays such as with the Auxiliary telescopes of VLTI. Figure 2.6 shows that, for a given zoom range, the compared VTDs from large and small deformation theories present less deviations than for Type 2. In the following example with a VCM in quenched stainless steel Fe87 Cr13. A positive central force generated convex shapes. The thickness t was derived by solving $\mathcal{T}_{20}$ in system (2.32) for the design value f/Ω = f/6 and a zoom-range [f/∞–f/4.5]. Before optical surfacing, the theoretical thickness $t\,(r)$ was increased by a constant extra-thickness and the rear side of the mirror executed by a numeric command lathe (Table 2.2).

Table 2.2 Thickness $t^*(r)$ of a Type 2 VCM before plane surfacing. Zoom range [f/∞ – f/4.5]. At the VCM edge, the radial thickness of the cylinder-collaret is 25 μm. t^* includes an extra-thickness of 5 μm (LOOM)

r	0.1	1	2	3	4	5	6	7	7.9	8^+	12
t^*	515	410	359	320	286	253	217	171	135	5,000	5,000

[r: mm, t^*: μm]

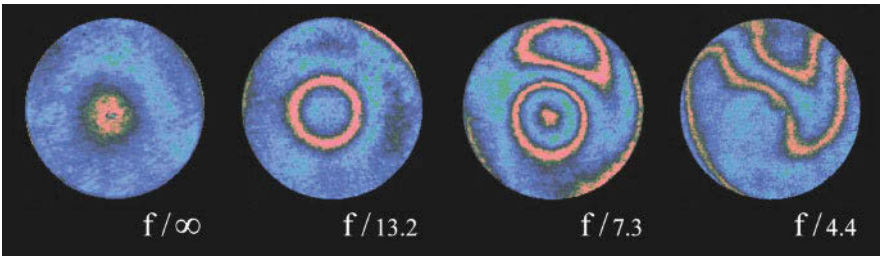

Fig. 2.14 Optical tests of a Type 2 VCM with respect to concave calibers. Zoom range f/∞−f/4.5. He-Ne patterns for full aperture $2a = 16$ mm. The central force is varied from 0 to 5.85 daN (LOOM)

For this zoom-range, the plastic deformation remains negligible and does not requires a compensation of the thickness distribution. After prestressing and plane surfacing, interferometric tests were carried out by use of Fizeau lenses of discrete curvatures and a ball-screw actuator driven by an encoded motorized system (Fig. 2.14).

2.7 Plasticity and Hysteresis

Because of the very large zoom range developed with "cycloid" type VCMs for 8 m aperture recombined telescopes (VLTI), it was found necessary to take under consideration the *plastic deformation* as well as the *hysteresis deformation loop* of the metal substrate. While plasticity goes back to the dawn of time, the discovery of hysteresis is due to J.A. Ewing in the 1880s.

A compensation of the plastic deformation and a hysteresis loop model can be determined in order to increase (i) the geometrical accuracy of the optical curvatures and (ii) the resolution of the curvature control. The plastic deformation error is corrected in the mirror figuring process, while hysteresis errors are compensated by the *closed-loop control system*.

2.7.1 Stress-Strain Linearization and Plasticity Compensation

• **Extended linear range:** For metallic alloys, the *Ewing-Muir process* [16] allows one to extend the linear range of the stress-strain relation. This *plastic tightening*, in French *raidissement plastique*, applies to the VCM substrates in quenched Fe87 Cr13 alloy. The process consists of prestressing the substrate at $\sigma_{\mathrm{p.s}}$ slightly higher than the working tensile maximum stress $\sigma_{t\,\max}$. Figure 2.15 displays the process in the case of an elongated rod. After applying a pre-stressing at $\sigma_{\mathrm{p.s}}$, the new length at rest becomes permanently increased, but for next loadings laying under $\sigma_{\mathrm{p.s}}$ the stress-strain law has been extended while remaining linear.

The prestressing applied to Type 1 VCMs (design in Table 2.1) was typically $\sigma_{\mathrm{p.s}} = 70\,\mathrm{daN.mm^{-2}}$ corresponding to a loading $q = 8.25\ \mathrm{daN.cm^{-2}}$. After final polishing, the VCMs operate up to a tensile maximum stress $\sigma_{t\,\max} = 68.4\,\mathrm{daN.mm^{-2}}$ corresponding to a loading $q_{\max} = 8.05\,\mathrm{daN.cm^{-2}}$ for the maximum permissible curvature $C_{\max}$.

Let C_0 be the initial curvature of a never stressed VCM and C_0^* its final curvature at rest after prestressing. The curvature difference due to *plasticity* is

$$\Delta C_{\mathrm{Plas}} = C_0^* - C_0\,. \tag{2.50}$$

He-Ne interferograms in Fig. 2.16 display the VCM shapes during the prestressing cycle of a previously unstressed VCM. The optical figures are recorded with

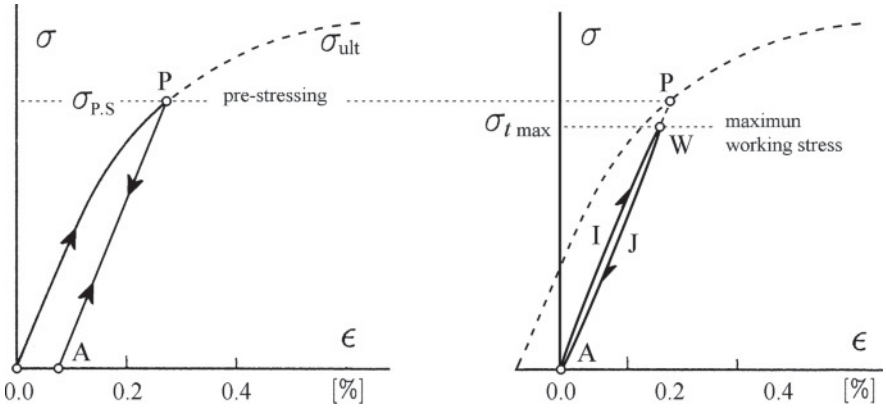

Fig. 2.15 Plasticity and hysteresis of quenched Fe87 Cr13 alloys. *Left*: Stress-strain diagram, Ewing-Muir linearization by prestressing. *Right*: Hysteresis loop in extended elastic domain after prestressing (the width of the loop is exagerated for clarity of the figure)

respect to reference lens calibers that are concave spheres of discrete curvature. These are mounted onto a wheel facing the VCM in a Fizeau mounting.

In a first approximation, the difference between the initial and final interferograms shows that the plastic deformation is of quadratic form

$$z_{\text{Plas}} \propto r^2 . \tag{2.51}$$

From Type 1 VCMs built with the design parameters in Fig. 2.4, the maximum tested elastic sag was $z_{\text{Elas}} = -381\,\mu\text{m}$ for the last caliber $R = 84\,\text{mm}$; the mean value of the measured plastic sags was $z_{\text{Plas}} = -14\,\mu\text{m}$. Thus, the typical *plasto-elastic deformation ratio* is

$$z_{\text{Plas}}/z_{\text{Elas}} \equiv (C_0^* - C_0)/(C_{\max} - C_0) = 3.67 \pm 0.15\,\% . \tag{2.52}$$

These results can be used for analysis with a plasticity theory (Lubliner [40]) for model investigations. Given the stress distribution of σ_r (Fig. 2.4), that is also of cycloid-like form, the plastic deformation appears near the substrate faces from mirror axis to a radius about half the aperture, $r \approx a/2$.

In order to compensate for the effect induced by the plastic deformation, the following conditions apply (Lemaitre et al. [38]):

• **Plasticity Compensation:** *Assuming a VCM figured quasi-flat with curvature C_0 at rest, which becomes $C_0^\star$ at rest after prestressing, and denoting $\Delta_{\text{Plas}} = C_0^\star - C_0$,*

1 → *if the optical figurings are always executed at same curvature before and after pre-stressing,*

2 → *and if the rear side of the substrate $Z_{\text{RS}}(r)$ is defined by the co-addition of the thickness distribution (elasticity term) and of a lens shape (plasticity term) following the sign of loading q as*

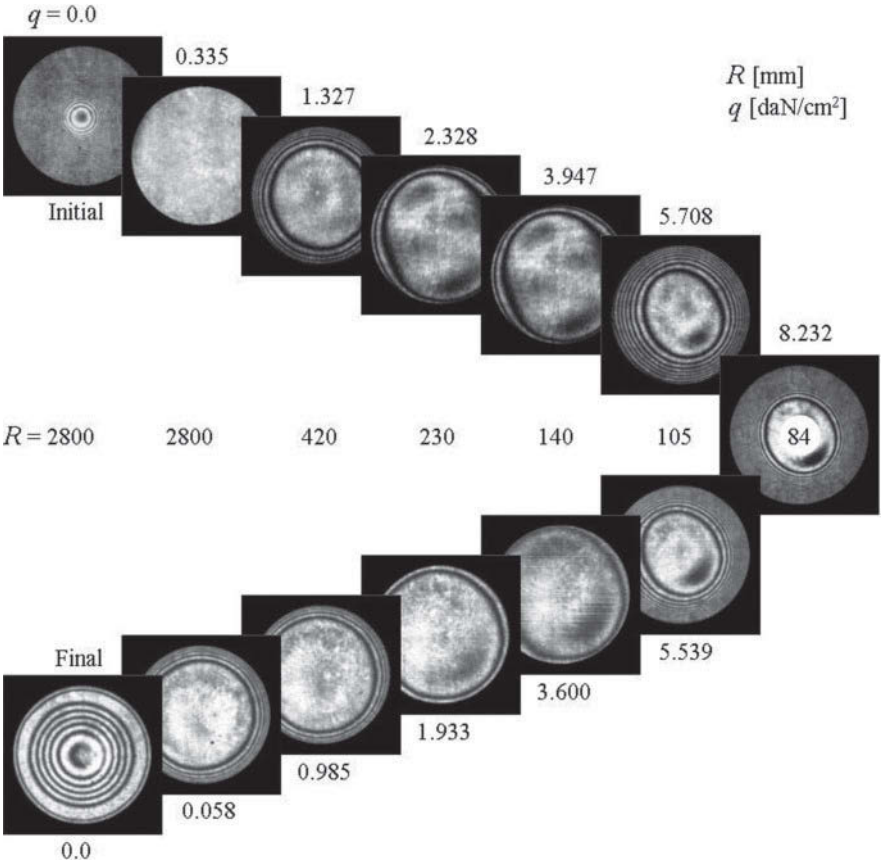

Fig. 2.16 He-Ne fringes with respect to calibers (R) and loads (q) of a VCM – Type 1 VTD-form – during *prestressing loop*. Plastic deformation is derived from the two patterns on left. The mirror is then resurfaced to a plane figure at $q = 0$. These VCMs of zoom range ($f/\infty - f/2.5$) are the core of cat's eye carriages of the VLTI eight delay lines (LOOM)

$$Z_{\mathrm{RS}} = t(r) - \Delta C_{\mathrm{Plas}}\,(a^2 - r^2)/2 \quad \textit{for} \quad q > 0 \;\; \textit{i.e.} \forall\, C < 0\,, \quad \textit{or} \tag{2.53a}$$

$$Z_{\mathrm{RS}} = t(r) + \Delta C_{\mathrm{Plas}}\, r^2/2 \qquad \textit{for}\; q < 0 \;\; \textit{i.e.} \forall\, C > 0\,, \tag{2.53b}$$

then the optimal properties of the VCM design with the large deformation theory are recovered.

These conditions can be realized by the construction and prestressing tests of preliminary prototypes allowing the determination of the lens shaped correction. Hence, the *plasticity correction* was set up in the final design of Type 1 VCMs, following (2.53a), which generates a zoom range with all negative curvature ($\forall\, C <$

0). This correction is included into the thicknesses $t^*(r)$ of Table 2.1 with $C_0 = 0$, $C_0^* = -0.44\,10^{-3}\,\mathrm{mm}^{-1}$ and $\Delta C_{\mathrm{Plas}} = C_0^\star - C_0 = C_0^\star$.

2.7.2 Hysteresis Compensation and Curvature Control

In Sect. 2.2, we have shown from the large deformation theory that the representation of the loading as a function of the flexure ratio is not linear (2.36) but expressed by an odd series in z/t_0. For Type 1 VCMs of zooming range [f/∞–f/2.5] deformed by air pressure, this representation provides a convenient accuracy by limiting the power series development up to $i = 5$. Considering the curvature C instead of the flexure ratio, the *load-curvature* relationship derived from (2.36) can be represented by (Ferrari et al. [22])

$$q = \beta_1 (C - C_0) + \beta_3 (C - C_0)^3 + \beta_5 (C - C_0)^5 , \tag{2.54}$$

where β_i are coefficients, C_0 the mirror curvature at rest and $\forall\, C < 0$.

For large deformations, metal substrates show a *flexural hysteresis*:

1 → *During the de-loading, the same curvatures as during loading are obtained by lower applied loads.*

2 → *After the loading and subsequent de-loading sequence, the initial and final curvatures are identical.*

The largest of the hysteresis loops is the path AIWJA (Fig. 2.14 *Right*), where the extremal working point W of maximum load $q_{\max}$ and curvature $C_{\max}$ is reached. Considering a loading sequence up to q_{seq}, and provided $q_{\mathrm{seq}} \le q_{\max} < q_{\mathrm{p.s}}$ such as defined from prestressing, the above load-curvature relationship is only valid for increasing pressures; when decreasing the load from a q_{seq} loading, the β_i coefficients become slightly different. Let $\overline{\beta}_i\big|_{\mathrm{seq}}$ be those coefficients. Given a curvature C, the load difference Δq between the increasing and decreasing pressures is a function of the maximum pressure q_{seq} or of the associated curvature C_{seq} reached in the going up sequence. The *hysteresis amplitudes* Δq, increasing with higher deformation sequences, are also represented by fifth-order odd polynomials

$$\Delta q\,\big|_{\mathrm{seq}} = \beta_1^* (C - C_0) + \beta_3^* (C - C_0)^3 + \beta_5^* (C - C_0)^5 , \tag{2.55}$$

with

$$\beta_i^* = \beta_i - \overline{\beta}_i\big|_{\mathrm{seq}} .$$

Remaining under the maximum working stress defined by the prestressing (Sect. 2.6.1), measurements have been carried out on 12 cycloid-type VCMs having a zoom-range [f/∞–f/2.5]. Hysteresis amplitudes were determined by Shack-Hartmann optical tests for loading sequences $q_{\mathrm{seq}} < q_{\max}$. Considering a representation of the hysteresis Δq in function of the load q instead of the curva-

ture, we obtain the form

$$\Delta q\,\big|_{\rm seq} \;=\; \delta_1\, q + \delta_3\, q^3 + \delta_5\, q^5\,, \qquad q \le q_{\rm seq} \le q_{\rm max}\,, \tag{2.56}$$

where δ_i coefficients are deduced from series (2.54) and (2.55).

From the (2.56) form, we can model all the hysteresis loops from simple properties. By definition, given a sequence, the hysteresis is null at the maximum load of the sequence, i.e. at $q = q_{\rm seq}$. In addition, the results from Shack-Hartmann tests show that the slopes of the hysteresis loops at $q = 0$ and $q = q_{\rm seq}$ are *opposite* (Ferrari [22]). Then, we have the two conditions

$$\Big[\Delta q\,\big|_{\rm seq}\Big]_{q\,=\,q_{\rm seq}} \;=\; 0\,, \qquad \Big[\frac{d}{dq}\,\Delta q\,\big|_{\rm seq}\Big]_{q\,=\,q_{\rm seq}} \;=\; -\Big[\frac{d}{dq}\,\Delta q\,\big|_{\rm seq}\Big]_{q\,=\,0}\,,$$

which entails

$$\delta_3 \;=\; -\,\frac{3}{2q_{\rm seq}^2}\;\delta_1 \quad \text{and} \quad \delta_5 \;=\; \frac{1}{2q_{\rm seq}^4}\;\delta_1\,. \tag{2.57}$$

The third condition to determine δ_1 is provided by the coordinates of the maximum amplitude. The results from Shack-Hartmann tests show that the slope at the origin is of the form

$$\delta_1 \;=\; a_1\, q_{\rm seq} \,+\, a_3\, q_{\rm seq}^3\,, \tag{2.58}$$

where a_1 and a_3 are coefficients. This allows one to construct a hysteresis grid model from the locus of the maximums, i.e. the coordinates of antinode A points. Therefore, the *hysteresis amplitude grid* for any sequence up to $q_{\rm seq}$ is defined by

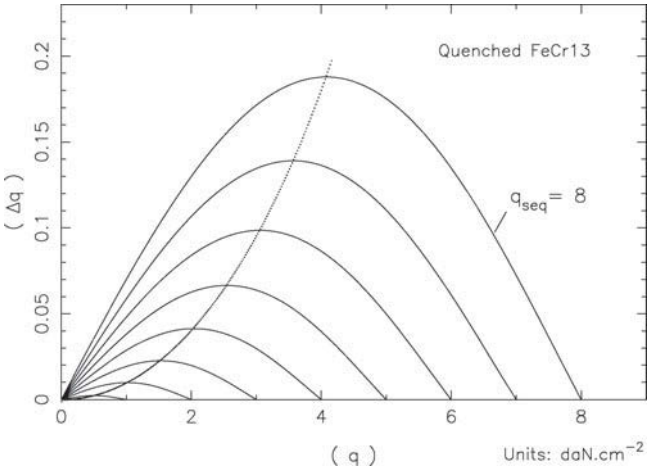

Fig. 2.17 Hysteresis $\Delta q(q)$ vs loading sequences $q_{\rm seq}$. Cycloid-like VCM – VTD Type 1 – actuated by air pressure. At $q_{\rm max} = 8$ daN.cm^{-2}, the radial stress is $\sigma = 68$ daN.mm^{-2} and the hysteresis amplitude $\Delta q/q_{\rm sec}$ reach 2.3% [38]

$$\Delta q\,\big|_{\rm seq} \;=\; \frac{1}{2}\left(a_1\, q_{\rm seq} \;+\; a_3\, q_{\rm seq}^3\right)\left(2 - \,3\frac{q^2}{q_{\rm seq}^2} + \frac{q^4}{q_{\rm seq}^4}\right) q\,, \tag{2.59a}$$

$$\text{with Antinodes}\quad \begin{cases} q_{\rm A}\big|_{\rm seq} \;=\; \kappa_1\, q_{\rm seq}\,, \\ \Delta q_{\rm A}\big|_{\rm seq} \;=\; \kappa_1\,\kappa_2\left(a_1\, q_{\rm seq}^2 + a_3\, q_{\rm seq}^4\right), \\ \kappa_1 \;=\; \left[(9-\sqrt{41})/10\right]^{1/2} \;=\; 0.5095, \\ \kappa_2 \;=\; (13+3\sqrt{41})/50 \;=\; 0.6441. \end{cases} \tag{2.60a}$$

The hysteresis curves are represented by the first positive part of five real-root curves (Fig. 2.17). The locus of the antinodal A-points is a biquadratic curve (Fig. 2.17 *Dotted line*). All these curves are determined from (2.59a) and set (2.59b) with coefficient values

$$a_1 \;=\; 7.65\;10^{-3}\,\mathrm{cm}^2\cdot\mathrm{daN}^{-1} \quad \text{and} \quad a_3 \;=\; 2.05\;10^{-5}\,\mathrm{cm}^6\cdot\mathrm{daN}^{-3}.$$

In order to achieve the best resolution of curvature control, this *hysteresis compensation model* is included in the VCM curvature *closed-loop control system* at the same level as the positioning control of the cat's eye translation.

References

1. J.M. Beckers, Field of view considerations for telescope arrays, SPIE Proc., **628**, 255 (1986)
2. J.M. Beckers et al., The VLTI implementation plan, ESO/VLT Report No. 59b (1989)
3. J.M. Beckers, Interferometric imaging with the VLTI, J. Optics (Paris), **22**, 73 (1991)
4. R.N. Bracewell, in *The Fourier Transform and Its Applications*, McGraw-Hill ed., New York (1965)
5. J.W. Brault, Fourier transform spectroscopy, in *High Resolution in Astronomy*, 15th Advanced Course, SAAS-FEE, 1–62 (1985)
6. R. Hanbury Brown, Measurement of stellar diameters, Ann. Rev. Astron. Astrophys., **6**, 13–38 (1968)
7. P. Casal, C. Fayard, B. Authier, Calculations of the elastic deformations of revolution membranes, Appl. Opt., **20**(11), 1983–1989 (1981)
8. A.A. Christy, Y. Ozaki, V.G. Gregoriou, in *Modern Fourier Transform Infrared Spectroscopy*, Elsevier ed., ISBN 0444 500 448, (2001)
9. P. Connes, Astronomical Fourier spectroscopy, Ann. Rev. Astron. Astrophys., **8**, 209–230 (1970)
10. P. Connes, G. Michel, Astronomical Fourier spectrometers, Appl. Opt., **14**, 9, 2067–2084 (1975)
11. S.P. Davis, M.C. Clark, J.W. Brault, in *Fourier Transform Spectroscopy*, Academic Press, San Diego ISBN 0120 425 106 (2001)
12. F. Derie, VLTI delay lines: Design, development and performance requirements, in *Interferometry in Optical Astronomy*, SPIE Proc., **4006**, 25–30 (2000)
13. T. Dohi and T. Suzuki, Appl. Opt., **10**, 1137 (1971)
14. K. Dohlen, Design of a FTS for environmental surveillance, Doctoral dissertation, University of London (1994)

15. K. Dohlen, Interferometric spectrometer for liquid mirror survey telescopes, in *Optical Telescopes of Today and Tomorrow*, SPIE/ESO Proc., **2871**,1359–1364 (1997)
16. J.A. Ewing, *The Strength of Materials*, Cambridge Univ. Press, 2nd ed., (1906). See also S.P. Timoshenko, *Résistance des Matériaux*, Dunod edt., Paris, 365–366 (1968)
17. M. Ferrari, G.R. Lemaitre, Analysis of large deflection zoom mirrors for the ESO VLTI, Astron. Astrophys. **274**, 12–18 (1993)
18. M. Ferrari, Optique active et grandes déformations élastiques, Doctoral dissertation, University Aix-Marseille I (1994)
19. M. Ferrari, F. Derie, B. Delabre, J.-M. Mariotti, VLTI's VCMs – Pupil transfer inside the delay line cat's eye, ESO Report No VLT-TRE-ESO-15220-1509 (1997)
20. M. Ferrari, Development of variable curvature mirrors for the delay lines of the VLTI, Astron. Astrophys. Suppl. Ser., **128**, 221–227 (1998)
21. M. Ferrari, G.R. Lemaitre, S. Mazzanti, P. Lanzoni, F. Derie, VLTI pupil transfer: Variable curvature mirrors [10], Final results and performances, in *Astronomical Telescopes and Instrumentation*, SPIE Proc., **4006**, 104–116 (2000)
22. M. Ferrari, S. Mazzanti, G.R. Lemaitre, J. Lemerrer, P. Lanzoni, P. Dargent, F. Derie, A. Huxley, A. Wallanders, Variable curvature mirrors - Implementation in the VLTI delay lines for field compensation, in *Interferometry for Optical Astronomy* II, SPIE Proc., **4838**, 1155–1162 (2002)
23. A. Glindeman et al. The VLT Interferometer, in *Interferometry in Optical Astronomy*, SPIE Proc., **4006**, 2–12 (2000)
24. E. Hugot, Optique astronomique et élasticité – Ph. D., Université de Provence – Aix Marseille I, Chap. 4 (2007)
25. P. Jacquinot, C. Dufour, J. Rech. CNRS, Lab. Bellevue (Paris), **6**, 91 (1948)
26. P. Jacquinot, J. Opt. Soc. Amer., **54**, 761 (1954)
27. B. Koehler, C. Flebus, VLT auxiliary telescopes, in *Interferometry in Optical Astronomy*, SPIE Proc., **4006**, 13–24 (2000)
28. D. Korsch, in *Reflective Optics*, Academic Press Inc., 173 (1991)
29. M. Krautter, Aplanatic two-mirror surfaces, in *Optical System Design, Analysis, and Production for Advanced Technology Systems*, SPIE Proc., **655**, 127–137 (1986)
30. O. von der Lühe, J.M. Beckers, R. Braun, The configuration of the VLTI on the Paranal site, in *High Resolution by Interferometry* **II**, ESO Conf. Proc., 959–968 (1991)
31. O. von der Lühe et al., A new plan for the VLTI, The Messenger, ESO ed., **87**, 8–14 (1997)
32. A. Labeyrie, Stellar interferometry methods, Ann. Rev. Astron. Astrophys., **16**, 77–102 (1978)
33. A. Labeyrie, Interferometry with arrays of large-aperture ground based telescopes, Proc. KPNO Conf. on *Optical and Infrared Telescopes for the 1990s*, **II**, 786–796 (1980)
34. C. Leinert, U. Graser, MIDI – The Mid-Infrared interferometer instrument for the VLTI, in *Astronomical Interferometry*, SPIE Proc., **3350**, 389–402 (1998)
35. G.R. Lemaitre, Élasticité et miroirs à focale variable, C. R. Acad. Sc. Paris, **282 B**, 87–89 (1976)
36. G.R. Lemaitre, French patent No 2343262 (1976), US patent No 4119 366 (1976)
37. G.R. Lemaitre, S. Mazzanti, M. Ferrari, P. Montiel, P. Lanzoni, Tulip-form variable curvature mirrors, in *Astronomical Interferometry*, SPIE Proc., **3350**, 373–379 (1998)
38. G.R. Lemaitre, M. Ferrari, S. Mazzanti, P. Lanzoni, P. Joulié, VLTI pupil transfer: Variable curvature mirrors [2], Plasticity, hysteresis and curvature control, in *Astronomical Telescopes and Instrumentation*, SPIE Proc., **4006**, 192–197 (2000)
39. G.R. Lemaitre, P. Montiel, P. Joulié, K. Dohlen, P. Lanzoni, Active optics and modified-Rumsey wide-field telescopes: MINITRUST demonstrators with vase- and tulip-form mirrors, Appl. Opt., **44**(34), 7322–7332 (2005)
40. J. Lubliner, in *Plasticity Theory*, MacMillan Publ. ed., New York (1991)
41. J.-P. Maillard, Seismology with Fourier transform spectrometer, Appl. Opt., **35**, 16, 2734–2746 (1996)
42. J.-P. Maillard, A super-imaging FTS for the VLTI, in *Scientific Drivers for* ESO *Future* VLT/VLTI *instrumentation*, ESO Conf., 193 (2002)

43. J.-M. Mariotti et al., The VLTI program: A status report, in *Astronomical Interferometry*, SPIE Proc., bf 3350, 800–806 (1998)
44. F. Merkle, Synthetic-aperture imaging with the VLT, Journ. Opt. Soc. Am., **A 5**(6), 904 (1989)
45. M. Mersenne, *Traité de l' Harmonie Universelle*, Paris (1636)
46. M. Mersenne, *L'Optique et la Catoptrique*, posthume publication, in *La Perspective Curieuse* by J.-F. Niceron, F. Langlois alias Chartres edt., Paris (1652)
47. L. Mertz, in *Transformation in Optics*, John Wiley and Sons ed., New York (1965)
48. A.A. Michelson, On the application of interference methods to astronomical measurements, Ap. J., **51**, 257–262 (1920)
49. D. Mourard et al., The GI2T/REGAIN interferometer, in *Astronomical Interferometry*, SPIE Proc., **3350**, 517–525 (1998)
50. F. Paresce, F. Delplancke, F. Derie, A. Glindemann, A. Richichi, M. Tarrenghi, Scientific objectives of ESO's PRIMA facility, in *Interferometry for Optical Astronomy* I, SPIE Proc., **4838**, 486–495 (2002)
51. M. Paul, Systèmes correcteurs pour réflecteurs astronomiques, Rev. Opt., **14**(5), 169–202 (1935)
52. N.J. Rumsey, A compact three-reflection astronomical camera, in *Optical Instruments and Techniques*, ICO 8 Meeting, London, Home Dickson edt., Oriel Press Newcastle, 514–520 (1969)
53. L. Seidel, Astron. Nachr., **43**, 289 (1856)
54. B.C. Smith, in *Fundamentals of Fourier Transform Infrared Spectroscopy*, CRC Press, Florida ISBN 0849 324 610, (1996)
55. E. Stephan, Sur les franges d'interférence observées avec de grands instruments, C. R. Acad. Sc., **76**, 1008–1010 (1873)
56. G.W. Stroke and A.T. Funkhauser, Physics Letters, **16**, 272 (1965)
57. A.P. Thorne, in *Spectrophysics*, Chapman and Hall ed., London (1988)
58. S.P. Timoshenko, S. Woinowsky-Krieger, *Theory of plate and shells*, McGraw-Hill ed., 396 (1976)
59. F. Vakili, I. Percheron, Beam combination and coherence tracking with diluted arrays, in *High Resolution by Interferometry* **II**, ESO Conf. Proc., 1247–1256 (1991)
60. A. Valentin, Fourier spectroscopy with a very long optical path length, Spectrochim. Acta, **51**-A(7), 1127–1142 (1995)
61. A. Valentin, A. Henry, The Fourier infrared spectrometer of Laboratoire de Physique Moléculaire et Applications, Paris-Jussieu, Internal report of LPMA/CNRS, Univ. P. & M. Curie, Paris (2002)
62. R.N. Wilson, Karl Schwarzschild and Telescope Optics, Karl Schwarzschild Lecture given to the German Astronomical Society, Bochum (1993), published in *Review of Modern Astronomy*, **7**, 1 (1994). See also *Reflecting Telescope Optics I*, Springer edt., 88 (1996)
63. L. Woltjer et al., Proposal for the construction of the 16-m VLT, ESO/VLT Report no. 57 (1987)

http://www.springer.com/978-3-540-68904-1

Astronomical Optics and Elasticity Theory
Active Optics Methods
Lemaitre, G.R.
2009, XXI, 575 p., Hardcover
ISBN: 978-3-540-68904-1